



Measurement of cesium $8^2P_J \rightarrow 6^2P_{J'}$ electric quadrupole transition probabilities using fluorescence spectroscopy

Jing Wang ¹, Yuki Miyamoto ², Hideaki Hara ², Minoru Tanaka ³, Motomichi Tashiro ⁴ and Noboru Sasao ^{2,*}

¹Graduate School of Natural Science and Technology, *Okayama University*, Okayama 700-8530, Japan

²Research Institute for Interdisciplinary Science, *Okayama University*, Okayama 700-8530, Japan

³Department of Physics, *Osaka University*, Toyonaka, Osaka 560-0043, Japan

⁴Department of Applied Chemistry, *Toyo University*, Kujirai 2100, Kawagoe, Saitama 350-8585, Japan



(Received 15 May 2024; revised 7 June 2024; accepted 14 June 2024; published 8 July 2024)

Fluorescence spectra of the $8^2P_J \rightarrow 6^2P_{J'}$ (J and $J' = 3/2, 1/2$) electric quadrupole transition of cesium atoms have been observed with a heated cesium vapor cell. We determined the ratio of the transition probabilities of $8^2P_J \rightarrow 6^2P_{J'}$ to $8^2P_J \rightarrow 5^2D_{3/2}$ by comparing their respective photon emission rates. The results are in good agreement with our theoretical calculations. These measurements provide crucial parameters for tests of the coherent amplification method and improve knowledge of cesium properties which are essential to dark matter detection through atomic transitions.

DOI: [10.1103/PhysRevA.110.012804](https://doi.org/10.1103/PhysRevA.110.012804)

I. INTRODUCTION

Revolutionary developments in atomic, molecular, and optical physics have been made in the past few decades [1]. Breakthroughs in experimental techniques, including laser cooling and trapping of atoms and buffer gas cooling for molecules, made it possible to perform precise tests of fundamental physics and observe new physics beyond the standard model [2–4]. For instance, spectroscopic analyses of the cesium (Cs) atom provided the most precise low-energy tests of parity nonconservation in the electroweak interaction [5–7]; the determination of the permanent electric dipole moment, a key indicator of violations of time-reversal and parity symmetries, has been accomplished [8–12] or is planned [13,14] for various atoms and molecules. The cornerstone of these measurements is the determination of the atomic or molecular parameters, including lifetimes, hyperfine structures, and transition matrix elements.

Another compelling driver is dark matter detection. Atomic or molecular transitions induced by the absorption of light dark matter particles, such as axions or dark photons, has come up in recent years [15,16], and several new experimental methods have been proposed [17,18]. However, due to the exceedingly low transition probability, an amplification method is needed. Coherent amplification of rare processes, as proposed [19] and examined by our group [20,21], emerges as a vital tool. This method holds the potential to significantly enhance processes like electric quadrupole transitions or two-photon transitions, thereby enabling study related to extremely weak phenomena, including dark matter absorption and neutrino mass spectroscopy [22].

We plan to do a dark matter search experiment using Cs atoms [23]: transitions induced by dark matter from $8^2P_{3/2}$ to $6^2P_{3/2}$ via $7^2D_{3/2}$ would be enhanced by coherence between

$8^2P_{3/2}$ and $6^2P_{3/2}$. We select Cs atoms as the target due to their simple electronic structure and well-studied atomic properties [24–33]. To determine the degree of coherence experimentally, we compare the coherence-amplified electric quadrupole transition $8^2P_{3/2} \rightarrow 6^2P_{3/2}$ rate with theoretical expectations; this requires knowledge of the transition matrix element in advance.

In this paper, we present a detailed report of the measurement of the Cs $8^2P_J \rightarrow 6^2P_{J'}$ electric quadrupole ($E2$) transition (magnetic dipole transition is much weaker than $E2$ transition because of the selection rules [34]). We performed laser-induced fluorescence spectroscopy of the transition within a heated vapor cell. We determined the ratio of the $E2$ transition rate to that of an electric dipole ($E1$) transition $8^2P_J \rightarrow 5^2D_{3/2}$ from the same excited state. Additionally, we calculated the $8^2P_J \rightarrow 6^2P_{J'}$ transition probabilities using configuration-interaction many-body perturbation theory (CI+MBPT) and compared them with experimental values. The agreement between theory and experiment is found to be good. This inherently weak transition serves as a crucial reference point for evaluating the amplification method and understanding potential background effects arising from other forbidden transitions.

The paper is organized as follows: in Sec. II, we present our experimental method and setup; in Sec. III we discuss data analysis and error budget; in Sec. IV, we show the results and compare them with theories; and finally, we present our conclusions in Sec. V.

II. EXPERIMENT

A. Atomic energy level

The partial energy-level diagram and the relevant transitions of Cs are illustrated in Fig. 1. In the experiment, a continuous-wave laser in resonance with the transition $6^2S_{1/2} \rightarrow 8^2P_J$ ($J = 3/2, 1/2$) at 388 and 389 nm is used to excite atoms to the 8^2P_J state. Successful excitation is

*Contact author: sasao@okayama-u.ac.jp

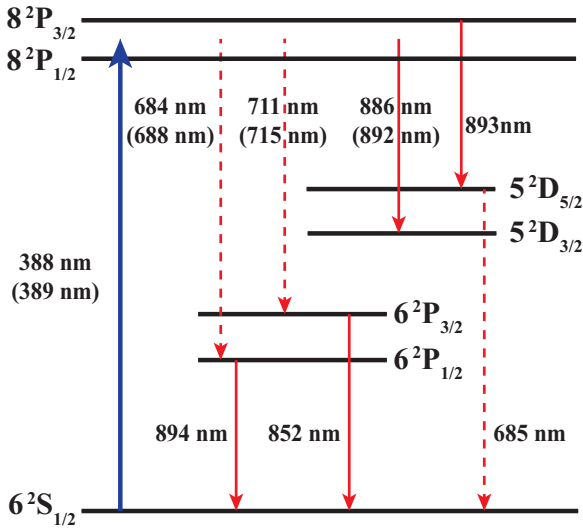


FIG. 1. Energy level of Cs and relevant transitions in the measurement. Electric dipole ($E1$) transitions are expressed with solid lines and quadrupole ($E2$) transitions with dashed lines. The arrows starting (ending) between the $8^2P_{3/2}$ and $8^2P_{1/2}$ indicate that they are from (to) one of these states, and their wavelengths for $8^2P_{3/2}$ ($8^2P_{1/2}$) are shown without (inside) parentheses. We excite the Cs atom from the $6^2S_{1/2}$ to 8^2P_J ($J = 3/2, 1/2$) state, and determine the ratio of the transition probabilities $8^2P_J \rightarrow 6^2P_{J'}$ to $8^2P_J \rightarrow 5^2D_{3/2}$ by comparing their photon emission rates.

detected by monitoring the Cs D_2 line ($6^2P_{3/2} \rightarrow 6^2S_{1/2}$) at 852 nm. The photons emitted through the $E2$ transitions $8^2P_J \rightarrow 6^2P_{J'}$ ($J' = 3/2, 1/2$) are then detected except for $8^2P_{1/2} \rightarrow 6^2P_{1/2}$. Additionally, the $E1$ transitions $8^2P_J \rightarrow 5^2D_{3/2}$ are detected as convenient references for determining the ratio of the transition probabilities. There are several reasons to choose the $8^2P_J \rightarrow 5^2D_{3/2}$ transitions as references.

(i) They originate from the same excited state, ensuring that the ratio is unaffected by potential errors arising from backgrounds such as photoionization or multiphoton transition processes.

(ii) We expect a reduced sensitivity to radiation-trapping effects.

(iii) Our detection system has higher efficiency at the wavelength of this transition than other lines.

The energy levels for $8^2P_{1/2}$ are similar to the case of $8^2P_{3/2}$. There are two differences, however, in addition to the transition wavelengths.

(i) Transitions $8^2P_{1/2} \rightarrow 5^2D_{5/2}$ and $8^2P_{1/2} \rightarrow 6^2P_{1/2}$ do not satisfy the $E1$ and $E2$ selection rules [34], so they are outside of our intended sensitivity for measuring $E2$ transitions.

(ii) The transition strength of $6^2S_{1/2} \rightarrow 8^2P_{1/2}$ is smaller than that of $8^2P_{3/2}$ by a factor of ≈ 4 [29], thus stronger laser intensity is required to have enough signal-to-noise ratio, especially for the forbidden transition.

Finally, we note that the initial population distribution of $8^2P_{1/2,3/2}$ hyperfine states has no impact on the ratio of transition probabilities we measure since the final hyperfine states are summed up [35].

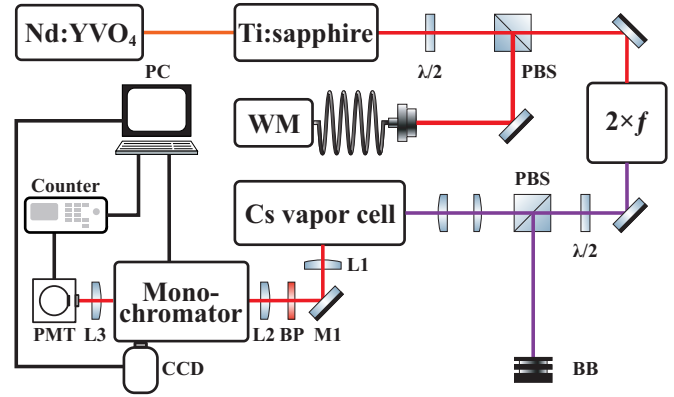


FIG. 2. Experimental setup. Nd:YVO₄, neodymium doped yttrium orthovanadate laser; Ti:sapphire, titanium sapphire laser; WM, wave meter; $2 \times f$, frequency doubling unit; PBS, polarizing beam splitter; $\lambda/2$, half-wave plate; BB, beam block; BP, bandpass filter (see Table I); CCD, charge-coupled device; PMT, photomultiplier tube; L and M, lens and mirror.

B. Laser system

Figure 2 illustrates the experimental setup. A Ti:sapphire laser (Coherent, 899-21 Ring laser), pumped by a Nd:YVO₄ laser (Coherent, Verdi-10), produces an output of 1 W at 776 nm. This laser can be locked to its reference cavity with a frequency fluctuation of less than 10 MHz. A small fraction of this laser output is directed into a wave meter (HighFinesse, WS-7) for wavelength determination. The main part of the laser beam is directed into a frequency doubling unit (Coherent, MBD-200). The doubling unit is composed of a lithium triborate crystal within a bow-tie cavity and efficiently generates a UV beam with a frequency matching the $6^2S_{1/2} \rightarrow 8^2P_J$ transition. Under typical operating conditions, one obtains a linearly polarized UV beam with a power up to 60 mW at the exit of the doubling unit. A half-wave plate combined with a polarizing beamsplitter is employed to adjust the laser power. A telescope modifies the beam waist to $\omega_x \times \omega_y = 0.9 \times 1.7$ mm. The laser then goes through a 2.5-cm cylindrical Cs vapor cell (TRIAD Technologies, TT-CS-20X75-CW). The cell is heated by a heater (Thorlabs, GCH25-75) and temperature is maintained by a temperature controller (Thorlabs, TED200C) with a temperature fluctuation within 0.1°C.

C. Fluorescence detector

Fluorescence lights emitted at a right angle to the propagation direction of the laser are focused on the entrance slit of a 1200-groove/mm monochromator (Princeton Instruments, Acton SP2300i) through a set of optical components such as mirrors, lenses, and bandpass filters. The monochromator has two selectable output ports: one of them with an exit slit is connected to a photomultiplier tube (PMT Hamamatsu, R13456P), and the other with no exit slit is connected to a charge-coupled device (CCD) camera (Princeton Instruments, PIXIS-100). Normally PMT is cooled down to -30°C to reduce dark count rates. It has a multi-alkali-metal cathode with a good quantum efficiency ($\text{QE} \approx 6\%$) at around 700 nm where the forbidden transitions are located. The CCD camera

TABLE I. Wavelength (λ) regions scanned by this experiment and transitions of interests. The labels correspond to the labels in Fig. 3. Filter range indicates a wavelength region transmitted by filters of FEL490 and FES700 [label (a) row], FBH710-10 [label (b) row], and FEL490 and FES750 [label (d) and (e) rows], and all filters are from Thorlabs.

Label	Type	Scanned region λ (nm)	Transitions	Filter range λ (nm)
(a)	$E2$	682–687	$8^2P_{3/2} \rightarrow 6^2P_{1/2}$	[490, 700]
(b)	$E2$	708–714	$8^2P_{3/2} \rightarrow 6^2P_{3/2}$	[705, 715]
(c)	$E1$	884–896	$8^2P_{3/2} \rightarrow 5^2D_{3/2}$ $8^2P_{3/2} \rightarrow 5^2D_{5/2}$	
(d)	$E2$	684–689	$8^2P_{1/2} \rightarrow 6^2P_{1/2}$	[490, 750]
(e)	$E2$	713–718	$8^2P_{1/2} \rightarrow 6^2P_{3/2}$	[490, 750]
(f)	$E1$	891–896	$8^2P_{1/2} \rightarrow 5^2D_{3/2}$	

operated at -70°C has higher quantum efficiency than PMT over a wide range of wavelength regions of interest. While it cannot do photon counting, it serves as a fast and convenient detector for determining various resonance frequencies and their intensities. Outputs from the PMT are directed to a pulse counting system composed of a discriminator with a threshold set at approximately 0.8 photoelectron level and a digital counter (Keysight, 53230A). An online computer is employed to record PMT/CCD data and to manage the monochromator.

D. Experimental procedure

The experimental procedure is structured as follows. We first adjust the frequency of the Ti:sapphire laser to maximize the D_2 line (852 nm) yields using CCD. Actually, we lock the Ti:sapphire laser frequency to 386.607 65 THz for $8^2P_{3/2}$ excitation and 385.363 78 THz for $8^2P_{1/2}$ excitation [25,29]. After switching to the PMT, we set the entrance and exit slit widths of the monochromator to 20 and 450 μm . These parameters are kept unchanged throughout the entire experiment. The actual scanning procedure for a given wavelength range is as follows. The photon counts are recorded every 1 s (1 Hz) while the monochromator is scanning at the speed of 1 nm/min. After the signal scan, the background spectrum is also recorded by detuning the laser frequency to the off-resonance. It turns out that the background rate is less than 0.5 Hz. The whole process is repeated for ten cycles, requiring approximately 1 h for data collection of each wavelength range. The scanning is performed for both forbidden transitions and allowed transitions. See Table I for the actual scan regions.

For convenience, we refer to a set of spectra obtained according to the above procedure as a “run”. We actually took five runs, two for $8^2P_{3/2}$ and three for $8^2P_{1/2}$, over a period of ten days.

III. DATA ANALYSIS

A. Raw spectra for $8^2P_{3/2}$ measurement

For the excitation of the $8^2P_{3/2}$ state, the UV laser wavelength is set to 388 nm with a power of 20 mW, and the Cs vapor cell temperature is set to be 55°C . As described in the previous section, the basic quantities obtained in

the experiment are the photon counts on the PMT for different transitions. Figures 3(a)–3(c) show the raw spectra, each spectra being the background-subtracted counts averaged over ten cycles. Figure 3(a) is the spectra in the forbidden region around 684 nm. In addition to the expected transition of $8^2P_{3/2} \rightarrow 6^2P_{1/2}$ (left peak), another $E2$ transition $5^2D_{5/2} \rightarrow 6^2S_{1/2}$ (right peak) is observed. Figure 3(b) shows the $E2$ transition of $8^2P_{3/2} \rightarrow 6^2P_{3/2}$ while Fig. 3(c) shows the $E1$ transitions $8^2P_{3/2} \rightarrow 5^2D_{3/2}$, $8^2P_{3/2} \rightarrow 5^2D_{5/2}$, and $D_1(6^2P_{1/2} \rightarrow 6^2S_{1/2})$. Due to the existence of the photoionization effect, some population goes to the higher excited state (e.g., $9^2S_{1/2}$), and then decays to $8^2P_{1/2}$ state, so the $8^2P_{1/2} \rightarrow 5^2D_{3/2}$ transition (892 nm) is also observed. This population leakage is confirmed by the detection of other $9^2S_{1/2}$ transitions using CCD. But it is rather weak and has no influence on the final ratio. All the peaks are fitted by a Gaussian line-shape function with a linear background. The raw counts (the area underneath the peak) and their statistical error, denoted as $C(\lambda) \pm \Delta C$ for each transition λ , are extracted from the fitted parameters.

We note all of the peaks exhibit similar full width at half maximum (0.42 ± 0.05 nm), which is limited by the resolution of the monochromator. We also note that the center wavelengths of the peaks are shifted by 0.4 nm compared to the theoretical wavelength for all the transitions, which can be attributed to the outdated calibration of the monochromator, but this shift does not influence the transition probabilities, and is calibrated in Fig. 3.

B. Raw spectra for $8^2P_{1/2}$ measurement

For the $8^2P_{1/2}$ excitation, the wavelength of the UV laser was set to 389 nm. As mentioned before, the transition strength of $6^2S_{1/2} \rightarrow 8^2P_{1/2}$ is smaller, so we increased the UV laser power from 20 to 30 mW. Also, the temperature of the Cs vapor cell was increased to 65°C to increase the atom density. The remaining parts of the setup remained unchanged.

Figures 3(d)–3(f) show the raw spectra observed by the $8^2P_{1/2}$ excitation. As seen in Fig. 3(d), the $8^2P_{1/2} \rightarrow 6^2P_{1/2}$ transition with a wavelength of 688 nm is not observed as expected [34]. The small observed peak corresponds to the transition $5^2D_{5/2} \rightarrow 6^2S_{1/2}$.

C. Raw counts and efficiency corrections

As mentioned, raw counts $C(\lambda)$ for each transition with a wavelength λ are obtained by fitting a Gaussian function with a linear background. In the case that the fit results are unsatisfactory, i.e., $\chi^2/n_{\text{DOF}} > 1$ (n_{DOF} being the degree of freedom), the errors are enlarged so that $\chi^2/n_{\text{DOF}} = 1$. Table II summarizes the results of such fits for each run. From the table, it is found that the corresponding counts measured on different days fluctuate more than statistically expected most likely due to environmental temperature variation or laser conditions. See Sec. III D for more discussions. It is confirmed, however, that the ratios of counts, for example, normalized to 886-nm ($P_{3/2}$) or 892-nm ($P_{1/2}$) data, are statistically consistent with each other (within 2σ). We therefore average the observed

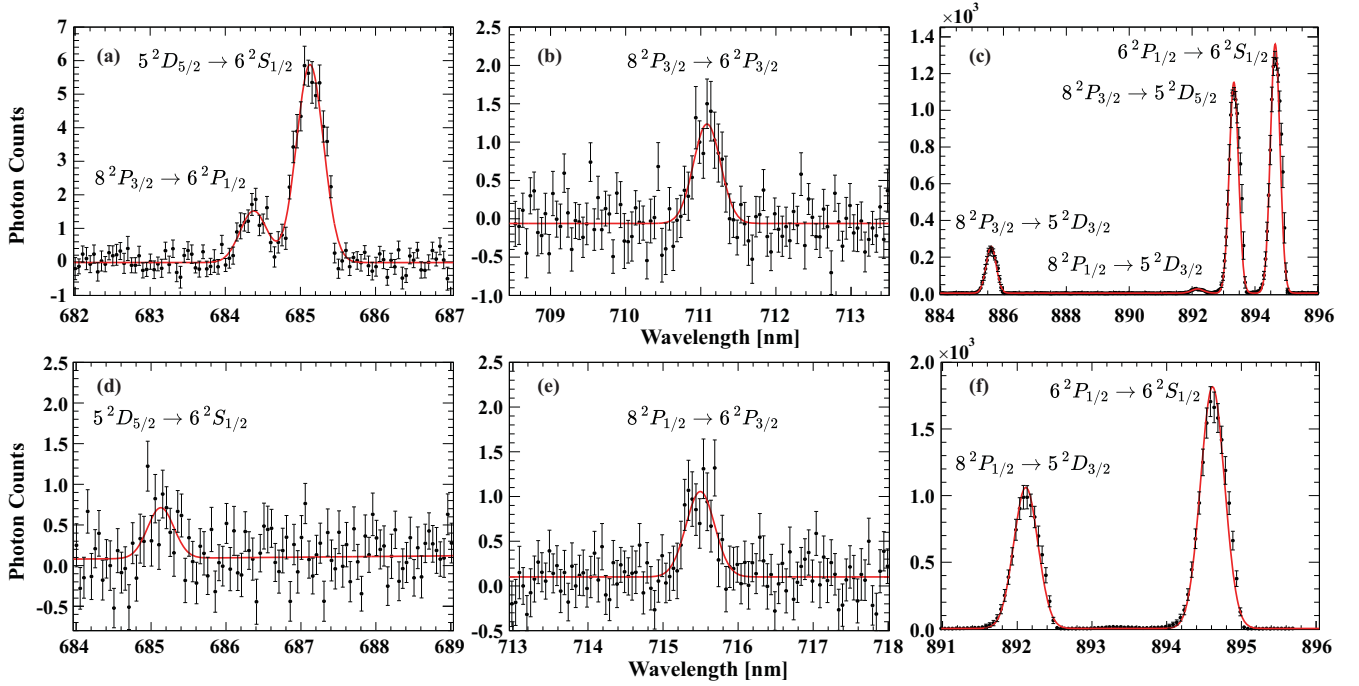


FIG. 3. Example of raw spectra. Experimental data are shown by black dots and fitting functions by red solid lines. The wavelength bin size is chosen to be 1/20 nm for all spectra. (a) E2 transitions $8^2P_{3/2} \rightarrow 6^2P_{1/2}$ and $5^2D_{5/2} \rightarrow 6^2S_{1/2}$. (b) E2 transition $8^2P_{3/2} \rightarrow 6^2P_{3/2}$. (c) E1 transitions $8^2P_{3/2} \rightarrow 5^2D_{3/2}$, $8^2P_{1/2} \rightarrow 5^2D_{3/2}$, $8^2P_{3/2} \rightarrow 5^2D_{5/2}$, $6^2P_{1/2} \rightarrow 6^2S_{1/2}$. (d) E2 transition $5^2D_{5/2} \rightarrow 6^2S_{1/2}$. (e) E2 transition $8^2P_{1/2} \rightarrow 6^2P_{3/2}$. (f) E1 transitions $8^2P_{1/2} \rightarrow 5^2D_{3/2}$, $6^2P_{1/2} \rightarrow 6^2S_{1/2}$.

counts over different runs. The results, denoted by $\langle C \rangle(\lambda)$, are shown in Table II.

The count $\langle C \rangle(\lambda)$ and its corresponding A coefficient are related to each other via

$$\langle C \rangle(\lambda) = N_{Cs} A(\lambda) \eta_{geo} \eta_{QE}(\lambda) \eta_{opt}(\lambda) t \quad (1)$$

where N_{Cs} is the number of excited Cs atoms, η_{geo} the geometrical acceptance, η_{QE} the quantum efficiency of PMT, η_{opt} the product of efficiencies of optical components from the cell to PMT, and t the data taking time at each point. Among the experimental variables in Eq. (1), N_{Cs} does not depend on λ . Similarly η_{geo} can be considered λ independent: this is confirmed by the studies using a simulation tool (see Sec. III D for details). Treating $N_{Cs} \eta_{geo}$ as λ independent, we define $R(\lambda) = \frac{\langle C \rangle(\lambda)}{t} \times \frac{\eta_{opt}^{(0)}}{\eta_{QE}(\lambda) \eta_{opt}(\lambda)}$, where $\eta_{opt}^{(0)} \equiv \eta_{opt}(900 \text{ nm})$, which is directly proportional to $A(\lambda)$. Table II shows the list of $\eta_{QE}(\lambda)$ and $\eta_{opt}(\lambda)$ normalized to $\eta_{opt}^{(0)}$. They are measured by the separate experiments described in the Appendixes.

D. Systematic uncertainty

We now investigate several potential sources of systematic uncertainties (errors) and study their impact on the measurement. Table III summarizes our error budget. They are classified into two categories: one is a random type (upper three rows) and the other is a scale error (lower four rows). The former introduces fluctuation in counts $C(\lambda)$ in addition to the statistical one. In contrast, η_{QE} , η_{opt} , and η_{geo} are proportional constants multiplied by the counts $C(\lambda)$ and thus their error may change R , not C . The monochromator performance difference also becomes sizable when the wavelength difference is large. They are categorized as ‘‘scale’’ errors and are treated differently from the random-type errors. Below we explain each of them in more detail.

1. Laser power fluctuations

One of the dominant contributors to experimental uncertainty is the fluctuations in laser power. These fluctuations

TABLE II. Raw counts (C) from different runs along with averaged counts $\langle C \rangle$, PMT quantum efficiency η_{QE} , and $\eta_{opt}/\eta_{opt}^{(0)}$.

λ (nm)	$C \pm \Delta C$			$\langle C \rangle \pm \Delta \langle C \rangle$	η_{QE} (%)	$\eta_{opt}/\eta_{opt}^{(0)}$
	Run 1	Run 2	Run 3			
684	$(1.39 \pm 0.12) \times 10^1$	$(1.47 \pm 0.13) \times 10^1$		$(1.43 \pm 0.09) \times 10^1$	12.2	1.37
711	$(1.10 \pm 0.16) \times 10^1$	$(1.17 \pm 0.13) \times 10^1$		$(1.14 \pm 0.10) \times 10^1$	10.6	1.50
886	$(2.01 \pm 0.07) \times 10^3$	$(2.28 \pm 0.09) \times 10^3$		$(2.15 \pm 0.06) \times 10^3$	0.194	0.950
893	$(8.49 \pm 0.17) \times 10^3$	$(1.02 \pm 0.02) \times 10^4$		$(9.35 \pm 0.13) \times 10^3$	0.100	0.976
715	$(9.88 \pm 1.94) \times 10^0$	$(1.19 \pm 0.15) \times 10^1$	$(9.13 \pm 1.82) \times 10^0$	$(1.03 \pm 0.10) \times 10^1$	10.5	1.27
892	$(9.26 \pm 0.41) \times 10^3$	$(9.47 \pm 0.38) \times 10^3$	$(8.58 \pm 0.35) \times 10^3$	$(9.11 \pm 0.22) \times 10^3$	0.110	0.972

TABLE III. Uncertainties on the photon counts, efficiencies, and monochromator acceptance

Source	Uncertainty (%)	Remark
Laser power	5	
Laser frequency	10	
Cell temperature	1	
Subtotal (random)	11.2	Added in quadrature
η_{QE}	5	
η_{opt}	5	
η_{geo}	2	
Monochromator	8	
Subtotal (scale)	10.9	Added in quadrature

amount to approximately 1 mW. The associated uncertainty can be quantified by measuring the photon counts at varying laser power levels. We measured the photon counts at 20, 25, and 30 mW and it is discerned that a 1-mW fluctuation introduces an uncertainty of 5% on the PMT counts.

2. Laser frequency drift

The laser system employed, a Ti:sapphire laser, is stabilized using a reference cavity. However, environmental factors such as optical table vibrations and temperature fluctuations can influence the length of the reference cavity, leading to a drift in the laser's frequency. During the course of the experiment, the laser frequency exhibits a drift of approximately 50 MHz. Notably, this frequency drift lies within the Doppler width. Although it has the potential to impact the ratio of hyperfine states in the excited state, analysis of the CCD camera's spectra reveals that the peak intensity remains stable with a variation of only 10%.

3. Cell temperature variations

Fluctuations in the temperature of the Cs vapor cell present another source of uncertainty which will influence the Cs density; the fluctuation is about 0.1 °C. We calculated the Cs density change from the Cs vapor pressure data [36], revealing a 0.7% change in Cs density for every 0.1 °C change around our experimental temperature. Additionally, we measured photon counts for the $8^2P_{1/2} \rightarrow 6^2P_{1/2}$ transition at temperatures of 55, 60, and 65 °C; the linear fitting shows a 0.3% change for every 0.1 °C. To be conservative, we set the uncertainty caused by the temperature fluctuation to be 1%.

4. Radiation trapping effect

This effect is most serious for the allowed transition, i.e., $8^2P_J \rightarrow 5^2D_{J'}$. To estimate the population of the $5^2D_{J'}$ state, we conducted rate equation simulations with the known transition probabilities from the NIST atomic spectra database [37], and found that it is comparable to that of the 8^2P_J state ($\approx 2\%$ of total Cs atoms). With this result and taking the Doppler effect into account, we estimated the mean free path of the photon using the cross section $\sigma(\lambda) = \frac{g_2 \lambda_0^2}{g_1} A_{21} g_D(\lambda)$, where g_1 and g_2 are the degeneracies of the $5^2D_{J'}$ and 8^2P_J states, λ_0 is the transition wavelength of $8^2P_J \rightarrow 5^2D_{J'}$, A_{21} is the A coefficient [38], and $g_D(\lambda)$ is a Gaussian line-shape

function with a width equal to the Doppler width Γ_D [39]. Considering the worst case of resonant absorption, $g_D(\lambda_0) = \frac{2\sqrt{\ln 2}}{\Gamma_D \times \sqrt{\pi}}$, we calculate the mean free path to be 48 cm for $8^2P_{3/2} \rightarrow 5^2D_{5/2}$, 300 cm for $8^2P_{3/2} \rightarrow 5^2D_{3/2}$, and 24 cm for $8^2P_{1/2} \rightarrow 5^2D_{3/2}$, which are much longer than the laser beam radius of 0.9×1.7 mm. We conclude that the trapping effect is negligibly small.

5. Uncertainties in η_{QE} and η_{opt}

As previously mentioned, η_{QE} and η_{opt} are measured in separate experiments. The uncertainties associated with these factors primarily arise from the nonreproducibility of photodiode spectra due to the relatively weak signal amplitude, resulting in larger background fluctuations compared to those of the PMT spectra. Both uncertainties are estimated to be 5%. See the Appendixes for details.

6. Uncertainties in η_{geo}

The geometrical factor η_{geo} depends, in principle, on λ through the dispersion effects of the lenses L1 and L2, leading to different spot sizes at the monochromator entrance slit. We performed a ray-tracing simulation using LIGHTTOOLS [40] and compared η_{geo} at two different wavelengths of 700 and 900 nm. Although the difference depends slightly on input geometrical parameters (such as distances between L1 and L2), it is at most 1.5%. Thus the uncertainty is conservatively taken to be 2%.

7. Monochromator performance difference

The monochromator may exhibit different performance across various wavelength ranges. Since the transitions we want to compare are located either around 700 or 900 nm, we categorized the peaks into two groups: one around 700 nm and another around 900 nm. We calculated the weighted averages of the peak widths in these two regions and compared them. It turns out that the relative difference is around 8% and the uncertainties of the average values are small compared to this difference. Therefore, we included this difference in our systematic uncertainties.

IV. RESULTS AND DISCUSSIONS

In this section, we first present the results of theoretical calculations of the A coefficients of the relevant transitions. Then we present our final experimental results and compare them with theories.

A. Theoretical calculation of A coefficients

In this paper, relativistic calculations of Cs energy levels and transition rates were carried out using CI+MBPT [41], which has been successfully applied to many atoms and ions. In this method, correlations among valence electrons are treated with the configuration-interaction method, while core-core and core-valence electron correlations are considered by the many-body perturbation theory. In this paper, we used the V^{N-1} approximation, i.e., we took the Xe core and considered a single valence electron. The basis set [25s25p25d25f25g25h] was employed, in which the

TABLE IV. Experimental and theoretical transition rates and their ratios.

Transition	λ (nm)	Type	Experiment		Theory			
			R (Hz)	Ratio	A (Hz) ^a	Ratio ^a	A (Hz) ^b	Ratio ^b
$8^2P_{3/2} \rightarrow 6^2P_{1/2}$	684	$E2$	$(8.56 \pm 0.54) \times 10^1$	$(7.32 \pm 0.50 \pm 1.14) \times 10^{-5}$	2.27	6.99×10^{-5}		
$8^2P_{3/2} \rightarrow 6^2P_{3/2}$	711	$E2$	$(7.17 \pm 0.63) \times 10^1$	$(6.13 \pm 0.56 \pm 0.96) \times 10^{-5}$	2.21	6.83×10^{-5}		
$8^2P_{3/2} \rightarrow 5^2D_{3/2}$	886	$E1$	$(1.17 \pm 0.03) \times 10^6$	1	3.20×10^4	1	4.93×10^4	1
$8^2P_{3/2} \rightarrow 5^2D_{5/2}$	893	$E1$	$(9.58 \pm 0.13) \times 10^6$	$8.19 \pm 0.24 \pm 0.92$	3.24×10^5	9.86	4.55×10^5	9.22
$8^2P_{1/2} \rightarrow 6^2P_{3/2}$	715	$E2$	$(7.72 \pm 0.75) \times 10^1$	$(9.10 \pm 0.91 \pm 1.42) \times 10^{-6}$	4.55	11.1×10^{-6}		
$8^2P_{1/2} \rightarrow 5^2D_{3/2}$	892	$E1$	$(8.51 \pm 0.21) \times 10^6$	1	4.11×10^5	1	5.66×10^5	1

^aThis paper.

^bSafronova *et al.* [38]. The A coefficient is calculated via $A = \frac{\omega_0^3}{3\pi\epsilon_0\hbar c^3} \frac{1}{2J+1} |(J\|\mathbf{er}\|J')|^2$ with the energy differences given by the NIST atomic spectra database [37].

$1s$ – $5s$, $1p$ – $5p$, and $1d$ – $4d$ orbitals are treated as core orbitals; the $6s$ – $8s$, $6p$ – $8p$, $5d$ – $7d$, and $4f$ orbitals are treated as the valence orbitals; and the remaining orbitals are considered as virtual orbitals. The core and valence orbitals were obtained by the Dirac-Hartree-Fock calculation, and the virtual orbitals were constructed based on these core and valence orbitals. The CI+MBPT calculation was performed using this basis set in combination with one- and two-electron radial integrals, and then the electric and magnetic multipole transition moments including the random-phase approximation corrections were evaluated based on the calculated wave functions.

The results of the calculations are listed in the sixth column of Table IV. For allowed transitions, there also exist calculations performed by Safronova *et al.* [38]: they are listed in the eighth column.

Uncertainties in the calculated $E2$ transition rates are rather difficult to estimate, because we only performed the CI+MBPT level of calculation, and did not perform higher level calculation as was done in Safronova *et al.* for error estimation. The difference of the $8^2P_{3/2} \rightarrow 5^2D_{5/2}$ $E1$ transition rate between our result and Safronova *et al.* is about 40%. If we can approximate that this difference is similar in the $E2$ transition, then the calculated result in Table IV may contain 40% uncertainty.

B. Results and comparison with theory

Our experimental results are summarized in Table IV. The fourth column is the efficiency-corrected counting rate (R) proportional to the A coefficient. The errors indicate only the statistical ones. The fifth column is R normalized to that of the allowed transition of $8^2P_J \rightarrow 5^2D_{3/2}$. Here the second error indicates a systematic error: for the forbidden transitions both random and scale errors, listed in Table III, are added in quadrature while for the allowed transitions only the random-type error is considered. Note that the scale error is relevant only to the different bands (700 vs 900 nm).

Our main results are

$$\frac{A(8^2P_{3/2} \rightarrow 6^2P_{1/2})}{A(8^2P_{3/2} \rightarrow 5^2D_{3/2})} = (7.32 \pm 0.50 \pm 1.14) \times 10^{-5}, \quad (2)$$

$$\frac{A(8^2P_{3/2} \rightarrow 6^2P_{3/2})}{A(8^2P_{3/2} \rightarrow 5^2D_{3/2})} = (6.13 \pm 0.56 \pm 0.96) \times 10^{-5},$$

$$1s-5s, 1p-5p, \text{ and } 1d-4d \text{ orbitals are treated as core orbitals;} \quad (3)$$

$$\frac{A(8^2P_{1/2} \rightarrow 6^2P_{3/2})}{A(8^2P_{1/2} \rightarrow 5^2D_{3/2})} = (9.10 \pm 0.91 \pm 1.42) \times 10^{-6}. \quad (4)$$

We are now able to compare these results with theoretical expectations shown in the seventh column of Table IV. Considering some uncertainties in the theoretical values, we conclude that the agreement between theory and experiment is satisfactory. In the case of the allowed transition $8^2P_{3/2} \rightarrow 5^2D_{5/2}$, our experimental value is consistent with two theoretical expectations within a 2σ range.

C. Forbidden transition $5^2D_{5/2} \rightarrow 6^2S_{1/2}$

In our setup, we also observed the transition $5^2D_{5/2} \rightarrow 6^2S_{1/2}$ with a wavelength of 685 nm, depicted in Figs. 3(a) and 3(d). This is another forbidden transition, and its A coefficient is already measured: $A = 22.22 \pm 0.24$ Hz [32]. To infer the experimental A coefficient of this transition requires knowledge of its parent ($5^2D_{5/2}$) population, which in turn demands a rate equation simulation. The result has uncertainty because the simulation needs all A coefficients leading to $5^2D_{5/2}$ and some of them are poorly determined. In addition, a two-photon ionization path may alter the population. Despite these restrictions, we carried out the simulation and found the A coefficient to be $22.2 \pm 0.60 \pm 3.45$ Hz when using the 893-nm transition as a reference. Considering various uncertainties, we conclude that our value is consistent with the reported value shown above: it enforces the reliability of our experiment.

V. SUMMARY

In this paper, we have presented an experiment that measured the Cs electric quadrupole ($E2$) transitions of $8^2P_J \rightarrow 6^2P_J$. To this end, we employed laser-induced fluorescence spectroscopy: a continuous-wave laser beam in resonance with the $6^2S_{1/2} \rightarrow 8^2P_J$ transition was used to excite Cs atoms in a heated vapor cell, and spontaneous emissions emitted to a right angle to the laser beam were detected with a photomultiplier tube after passing through a monochromator. We determined the ratio of the $E2$ transition rate to that of the

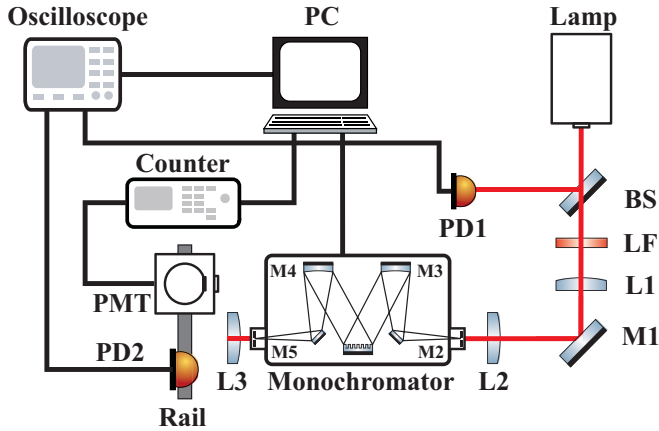


FIG. 4. Calibration experiment setup. BS, beamsplitter; LF, lamp filter (FEL600 for QE calibration; FBH710-10 or FBH900-10 for η_{opt} calibration, and all filters are from Thorlabs); other notations are consistent with those in Fig. 2.

electric dipole ($E1$) transition $8^2P_J \rightarrow 5^2D_{3/2}$ from the same excited state. Our main results are shown in Eqs. (2)–(4).

We also calculated the $8^2P_J \rightarrow 6^2P_J$ transition probabilities with CI+MBPT and compared them with the experimental values. The agreement between theory and experiment is found to be good.

This inherently weak transition serves as a crucial reference point for evaluating the coherent amplification mechanism and comprehending potential background effects arising from other forbidden transitions [23]. With this result, an axion and/or dark photon search is in progress.

ACKNOWLEDGMENTS

This work was supported by Japan Society for the Promotion of Science KAKENHI Grant No. 16H02136 (N.S.); Grants No. 21H00074, No. 18K03621, and No. 24K07018 (Mi.T.); Grant No. 23K22520 (Y.M.); and Grant No. 21H01112 (H.H.). The computation in this paper was partially performed at Research Center for Computational Science, Okazaki, Japan (Project No. 23-IMS-C070).

APPENDIX A: PHOTOCATHODE QUANTUM EFFICIENCY η_{QE}

The photocathode QE of PMT is one of the most important quantities since its differences for the signal (684–715 nm) and reference (886–893 nm) bands are expected to be large. We measured relative QEs experimentally and compared the results with those provided by the manufacturer. In this section, we describe our QE calibration procedure in detail.

For the QE calibration experiment, as shown in Fig. 4, we replaced the Cs vapor cell with a tungsten-halogen lamp (Ocean optics, DH-2000), which emits a broad spectra ranging from 350 nm to at least $1 \mu\text{m}$, with a power output of $> 1 \text{ W}$. The bandpass filter (BP) was removed and a long pass filter (LF, Thorlabs FEL600) was placed before L1 to prevent higher-order diffractions of the monochromator grating. We first adjusted the lamp intensity so that the PMT counting rate was less than 100 kHz to avoid possible saturation effects. We

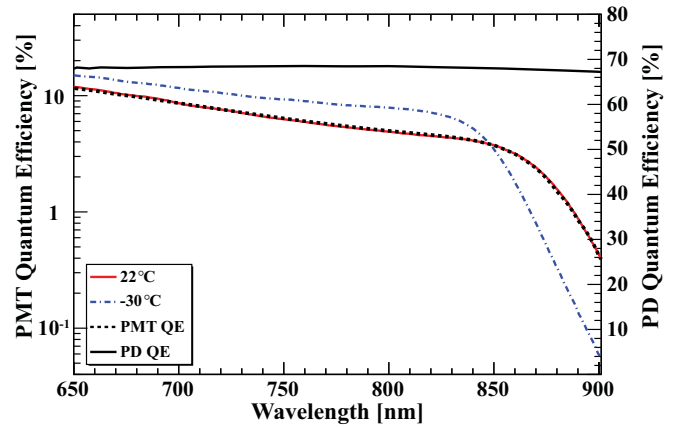


FIG. 5. Quantum efficiencies vs wavelength. Our measurement: PMT QE at room temperature (red solid) and at -30°C (blue dash-dotted). Hamamatsu measurement: PMT QE at room temperature (black dashed line) and PD QE at room temperature (black solid).

then measured the PMT rates by changing the monochromator wavelength from 590 to 920 nm at every 0.5 nm. The actual counts per point were greater than 400 Hz. Backgrounds, measured with the lamp blocked, were subtracted from the data. The procedure was repeated at different PMT temperatures: 22°C (room temperature) and $15, -10, -20,$ and -30°C . We also measured a spectrum with a photodiode (PD) (Hamamatsu, S2281) at room temperature by replacing PMT using a rail. Since the light intensity is rather weak for PD, so we use serial amplifiers (Hamamatsu, C9051-01 and Thorlabs, AMP200) to measure the spectra. All PMT measurements are sandwiched by PD measurements to ensure the stability of the lamp spectra. Note that the optics from the lamp to the detectors remained the same except for the neutral density filter (Thorlabs, ND10A) which was removed for PD to enhance the signal amplitude. Using the transmission spectra of ND10A, which was measured in a separate experiment, and the PD's QE provided by Hamamatsu [42], we could determine the lamp spectra at the exit of the monochromator, which was in turn used to determine PMT relative QEs.

Figure 5 shows our results: the QE at room temperature (red solid) and at -30°C (blue dash-dotted). Additionally, the QEs for the PD (black solid line), obtained from Hamamatsu's datasheet, and for the PMT (black dashed line), calibrated by the Hamamatsu factory, are also depicted. Note that our results are rescaled so that the room-temperature QE at 850 nm aligns with Hamamatsu's value. We find a good agreement between two room-temperature QEs of ours and Hamamatsu's. The main uncertainties of the QE measurement come from the reproducibility of PD spectra, which is found to be better than 5%.

Although not essential to our main experiment, we could measure the temperature coefficient of the cathode sensitivity as a byproduct. The result is shown in Fig. 6, where the vertical axis denotes $\frac{\Delta\eta_{\text{QE}}}{\eta_{\text{QE}}^{(0)}} = \frac{\eta_{\text{QE}}(T) - \eta_{\text{QE}}^{(0)}}{\eta_{\text{QE}}^{(0)}}$ with $\eta_{\text{QE}}^{(0)}$ being the room-temperature QE. We note the temperature values used so far are all nominal (the values displayed by the cooling unit). We measured the actual temperature inside the cooling unit with a pt100 sensor. The measurement results

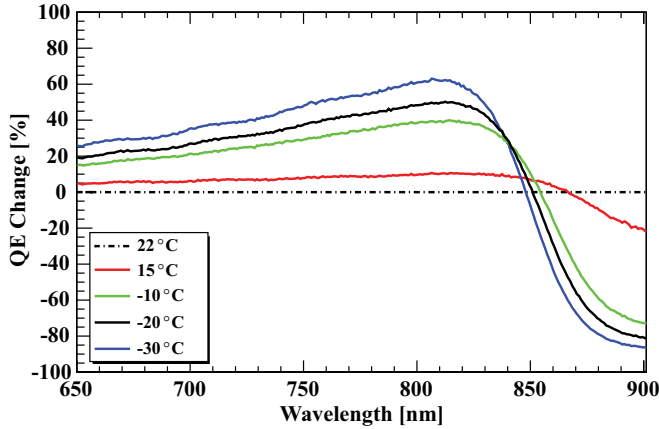


FIG. 6. Quantum efficiency change normalized to room temperature, i.e., $\Delta\eta_{QE}/\eta_{QE}^{(0)}$.

are 15.6°C (15°C), -7.9°C (-10°C), -16.5°C (-20°C), and -26.5°C (-30°C), where the values in parentheses are nominal ones.

APPENDIX B: OPTICAL COMPONENT EFFICIENCY η_{opt}

Another important quantity in Eq. (1) is η_{opt} . It represents a product of efficiencies of all optical components from the Cs cell to the detector, including lenses (L1–L3), mirrors (M1–M5), BP, and the grating. In this section, a calibration experiment is described, which measured $r = \frac{\eta_{opt}(710\text{ nm})}{\eta_{opt}^{(0)}}$, the

ratio of η_{opt} at the signal band (684–715 nm) and reference band (886–893 nm). As illustrated in Fig. 4, we inserted lamp bandpass filters (LF) with the transmission window of 710 ± 5 nm or 900 ± 5 nm at the exit of the lamp, and measured the intensity with PD right after the L1 and the exit of the monochromator. There was no BP in this setup.

The PD output after the LF of $\lambda_{LF} = (710\text{ nm or } 900\text{ nm})$ is proportional to $I(\lambda_{LF})\eta_{PD}(\lambda_{LF})$ while that at the monochromator exit is proportional to $I(\lambda_{LF})\eta_{PD}(\lambda_{LF})\eta_{opt}(\lambda_{LF})$, where I and η_{PD} denote the lamp intensity and the PD sensitivity, respectively. We deduced r from these four measurements (two different LFs at two different locations) and found it to be $r = 1.54$. Three corrections are applied to r obtained above to reach the values in Table II.

(i) The effect of the BP (as shown in Table I): we measured the transmission efficiency of each combination in a separate experiment.

(ii) The L1 lens effect: since the PD detector is placed downstream of L1 in the calibration setup, we must take into account the wavelength dependence of its transparency separately. Fortunately, the lens material (BK7) has flat transparency in this wavelength region: 92% at 710 nm and 94% at 900 nm (10 mm thick).

(iii) Wavelength dependence within the signal or reference bands: the main dependence comes from the grating efficiency. With the efficiency curve provided by the manufacturer [43], corrections are estimated. Uncertainty in η_{opt} comes from the nonreproducibility of PD spectra. Considering the results of η_{QE} calibration experiments, we assign 5% uncertainty to η_{opt} conservatively.

-
- [1] G. W. Drake, *Springer Handbook of Atomic, Molecular, and Optical Physics*, 2nd ed. (Springer, New York, 2023).
- [2] J. Ginges and V. V. Flambaum, Violations of fundamental symmetries in atoms and tests of unification theories of elementary particles, *Phys. Rep.* **397**, 63 (2004).
- [3] B. Roberts, V. Dzuba, and V. Flambaum, Parity and time-reversal violation in atomic systems, *Annu. Rev. Nucl. Part. Sci.* **65**, 63 (2015).
- [4] M. S. Safronova, D. Budker, D. DeMille, D. F. Jackson Kimball, A. Derevianko, and C. W. Clark, Search for new physics with atoms and molecules, *Rev. Mod. Phys.* **90**, 025008 (2018).
- [5] C. S. Wood, S. C. Bennett, D. Cho, B. P. Masterson, J. L. Roberts, C. E. Tanner, and C. E. Wieman, Measurement of parity nonconservation and an anapole moment in cesium, *Science* **275**, 1759 (1997).
- [6] M. A. Bouchiat, J. Guena, L. Hunter, and L. Pottier, Observation of a parity violation in cesium, *Phys. Lett. B* **117**, 358 (1982).
- [7] J. Guéna, M. Lintz, and M. A. Bouchiat, Measurement of the parity violating 6S-7S transition amplitude in cesium achieved within 2×10^{-13} atomic-unit accuracy by stimulated-emission detection, *Phys. Rev. A* **71**, 042108 (2005).
- [8] M. C. Weisskopf, J. P. Carrico, H. Gould, E. Lipworth, and T. S. Stein, Electric dipole moment of the cesium atom. a new upper limit to the electric dipole moment of the electron, *Phys. Rev. Lett.* **21**, 1645 (1968).
- [9] E. S. Ensberg, Experimental upper limit for the permanent electric dipole moment of Rb^{85} by optical-pumping techniques, *Phys. Rev.* **153**, 36 (1967).
- [10] C. Chin, V. Leiber, V. Vuletić, A. J. Kerman, and S. Chu, Measurement of an electron's electric dipole moment using Cs atoms trapped in optical lattices, *Phys. Rev. A* **63**, 033401 (2001).
- [11] B. Graner, Y. Chen, E. G. Lindahl, and B. R. Heckel, Reduced limit on the permanent electric dipole moment of ^{199}Hg , *Phys. Rev. Lett.* **116**, 161601 (2016).
- [12] ACME Collaboration, Improved limit on the electric dipole moment of the electron, *Nature (London)* **562**, 355 (2018).
- [13] T. Inoue, S. Ando, T. Aoki, H. Arikawa, S. Ezure, K. Harada, T. Hayamizu, T. Ishikawa, M. Itoh, Kato *et al.*, Experimental search for the electron electric dipole moment with laser cooled francium atoms, *Hyperfine. Interact.* **231**, 157 (2015).
- [14] C. Tang, T. Zhang, and D. S. Weiss, Improving sensitivity to magnetic fields and electric dipole moments by using measurements of individual magnetic sublevels, *Phys. Rev. A* **97**, 033404 (2018).
- [15] P. Sikivie, Axion dark matter detection using atomic transitions, *Phys. Rev. Lett.* **113**, 201301 (2014).
- [16] A. Arvanitaki, S. Dimopoulos, and K. Van Tilburg, Resonant absorption of bosonic dark matter in molecules, *Phys. Rev. X* **8**, 041001 (2018).
- [17] L. Santamaria, C. Braggio, G. Carugno, V. D. Sarno, P. Maddaloni, and G. Ruoso, Axion dark matter detection by laser

- spectroscopy of ultracold molecular oxygen: A proposal, *New J. Phys.* **17**, 113025 (2015).
- [18] G.-Y. Huang and S. Zhou, Probing cosmic axions through resonant emission and absorption in atomic systems with superradiance, *Phys. Rev. D* **100**, 035010 (2019).
- [19] N. Sasao and M. Yoshimura, New method of galactic axion search, *Eur. Phys. J. C* **78**, 949 (2018).
- [20] Y. Miyamoto, H. Hara, S. Kuma, T. Masuda, I. Nakano, N. Sasao, C. Ohae, M. Tanaka, S. Uetake, A. Yoshimi, K. Yoshimura, and M. Yoshimura, Observation of coherent two-photon emission from the first vibrationally excited state of hydrogen molecules, *Prog. Theor. Exp. Phys.* **2014**, 113C01 (2014).
- [21] Y. Miyamoto, H. Hara, T. Masuda, N. Sasao, M. Tanaka, S. Uetake, A. Yoshimi, K. Yoshimura, and M. Yoshimura, Externally triggered coherent two-photon emission from hydrogen molecules, *Prog. Theor. Exp. Phys.* **2015**, 081C01 (2015).
- [22] T. Masuda, H. Hara, Y. Miyamoto, N. Sasao, M. Tanaka, S. Uetake, A. Yoshimi, K. Yoshimura, and M. Yoshimura, *Recent Progress of Span Towards Neutrino Mass Spectroscopy* (Institute of Physics, University of Reading, Berkshire, 2016), p. 062043.
- [23] J. Wang, H. Hara, Y. Miyamoto, N. Sasao, and M. Tanaka, Dark matter search with coherent atoms (unpublished).
- [24] S. Pucher, P. Schneeweiss, A. Rauschenbeutel, and A. Dureau, Lifetime measurement of the cesium $5^2D_{5/2}$ state, *Phys. Rev. A* **101**, 042510 (2020).
- [25] J. A. Quirk, L. Sherman, A. Damitz, C. E. Tanner, and D. S. Elliott, Measurement of the hyperfine coupling constants and absolute energies of the $8p^2P_{1/2}$ and $8p^2P_{3/2}$ levels in atomic cesium, *Phys. Rev. A* **107**, 012807 (2023).
- [26] S. B. Bayram, P. Arndt, O. I. Popov, C. Güney, W. P. Boyle, M. D. Havey, and J. McFarland, Quantum beat spectroscopy: Stimulated emission probe of hyperfine quantum beats in the atomic Cs $8p^2P_{3/2}$ level, *Phys. Rev. A* **90**, 062510 (2014).
- [27] W. D. Williams, M. T. Herd, and W. B. Hawkins, Spectroscopic study of the $7p_{1/2}$ and $7p_{3/2}$ states in cesium-133, *Laser Phys. Lett.* **15**, 095702 (2018).
- [28] M. T. Herd, E. C. Cook, and W. D. Williams, Absolute frequency measurement of the $6D_{5/2}$ level of neutral ^{133}Cs using two-photon spectroscopy, *Phys. Rev. A* **104**, 042812 (2021).
- [29] Y.-W. Liu and P. E. G. Baird, Measurement of the cesium $6S_{1/2} \rightarrow 8P_{1/2}$ transition frequency, *Appl. Phys. B* **71**, 567 (2000).
- [30] E. A. Chan, S. A. Aljunid, N. I. Zheludev, D. Wilkowski, and M. Ducloy, Doppler-free approach to optical pumping dynamics in the $6S_{1/2} \rightarrow 5D_{5/2}$ electric quadrupole transition of cesium vapor, *Opt. Lett.* **41**, 2005 (2016).
- [31] T.-J. Chen, J.-E. Chen, H.-H. Yu, T.-W. Liu, Y.-F. Hsiao, Y.-C. Chen, M.-S. Chang, and W.-Y. Cheng, Absolute frequency of cesium $6S_{1/2} \rightarrow 6D_{3/2}$ hyperfine transition with a precision to nuclear magnetic octupole interaction, *Opt. Lett.* **43**, 1954 (2018).
- [32] S. Tojo, T. Fujimoto, and M. Hasuo, Precision measurement of the oscillator strength of the cesium $6^2S_{1/2} \rightarrow 5^2D_{5/2}$ electric quadrupole transition in propagating and evanescent wave fields, *Phys. Rev. A* **71**, 012507 (2005).
- [33] A. Markhotok, S. B. Bayram, A. Sieradzan, and M. D. Havey, Precision polarization measurements of the $6s^2S_{1/2} \rightarrow 6p^2P_j$ Rayleigh scattering spectrum in atomic Cs, *J. Appl. Phys.* **92**, 1613 (2002).
- [34] B. H. Bransden and C. J. Joachain, *Physics of Atoms and Molecules*, 2nd ed. (Pearson, Harlow, 2003), Eqs. (9.83c) and (9.84b).
- [35] D. A. Steck, Cesium D line data (2019), <http://steck.us/alkalidata>, Eq. (42).
- [36] C. B. Alcock, V. P. Itkin, and M. K. Horrigan, Vapour pressure equations for the metallic elements: 298–2500 K, *Can. Metall. Quart.* **23**, 309 (1984).
- [37] A. Kramida, Y. Ralchenko, J. Reader, and NIST ASD Team, NIST atomic spectra database (version 5.11) (2023), <https://physics.nist.gov/asd>.
- [38] M. S. Safronova, U. I. Safronova, and C. W. Clark, Magic wavelengths, matrix elements, polarizabilities, and lifetimes of Cs, *Phys. Rev. A* **94**, 012505 (2016).
- [39] C. J. Foot, *Atomic Physics*, 1st ed. (Oxford University, New York, 2005), Eq. (8.14).
- [40] Synopsis, LightTools Illumination Design Software (2024), <https://www.synopsys.com/optical-solutions/lighttools.html>.
- [41] M. G. Kozlov, S. Porsev, M. Safronova, and I. Tupitsyn, CI-MBPT: A package of programs for relativistic atomic calculations based on a method combining configuration interaction and many-body perturbation theory, *Comput. Phys. Commun.* **195**, 199 (2015).
- [42] Hamamatsu, Si photodiode with BNC connector (2023), https://www.hamamatsu.com/content/dam/hamamatsu-photronics/sites/documents/99_SALES_LIBRARY/ssd/s2281_series_kspd1044e.pdf.
- [43] Teledyne Princeton Instruments, Scanning monochromator datasheet (2007), https://optronis.com/wp-content/uploads/2017/03/SpectraPro_Rev_N3_5-19-14.pdf.